Journal of Materials Chemistry A

Accepted Manuscript

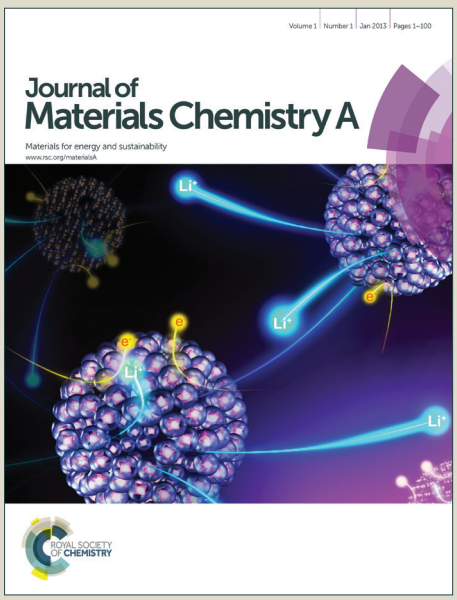

ROYAL SOCIETY OF CHEMISTRY

www.rsc.org/materialsA

Table of contents

A MOF composite GO/Zn-Co-ZIF/Nickel foam derived RGO/$ZnCo_2O_4$-ZnO-C/Ni sandwich-like anode exhibits excellent electrochemical performance as binder-free anode for LIBs.

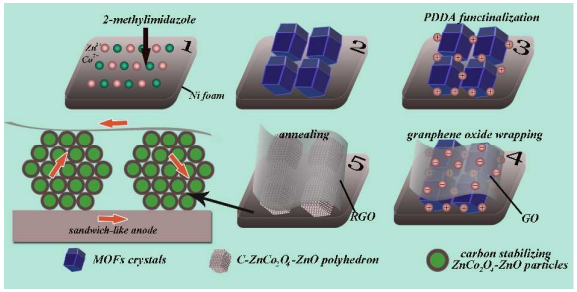

Sandwich-Like Reduced Graphene Oxide Wrapped MOF-Derived $ZnCo_2O_4$-ZnO-C on Nickel Foam as Anodes for High Performance Lithium Ion Batteries

Zhaoqiang Li, Longwei Yin*

Key Laboratory for Liquid-Solid Structural Evolution and Processing of Materials, Ministry of Education, School of Materials Science and Engineering, Shandong University, Jinan 250061, P. R. China

*To whom correspondence should be addressed. Tel.: + 86 531 88396970. Fax: + 86 531 88396970. E-mail: yinlw@sdu.edu.cn

Abstract A sandwich-like structure with reduced graphene oxide (RGO) wrapped MOF-derived $ZnCo_2O_4$-ZnO-C polyhedrons on nickel foam as an anode for high performance lithium ion batteries (LIBs), is for the first time reported via a simply growing MOFs on Ni foam, and wrapping of graphene oxide nanosheets on MOFs, then annealing under N_2 atmosphere. It should be noted that the MOF-derived porous products are composed of carbon-coated spinel $ZnCo_2O_4$-ZnO nanoparticle polyhedrons. When tested as anode for LIBs, the unique RGO/$ZnCo_2O_4$-ZnO-C/Ni sandwich-structured LIBs anodes exhibit superior coulombic efficiency, excellent cycling stability and rate capability. The in situ formed carbon layers outside the $ZnCo_2O_4$-ZnO act as not only conductive substrate but also buffer layer for volume changes. The open pores in $ZnCo_2O_4$-ZnO-C polyhedrons provide sufficient electrolyte as well as serve as cushion space to further alleviate volume changes. The RGO nanosheets act as a flexible protector to firmly fix polyhedrons on the Ni foam, as well as conductive substrate to wire up all the polyhedrons. The interconnected carbon layers and two high conductive substrates (RGO and Ni foam) together form an unhindered highway for charge transfer during discharge/charge processes, promising good electrochemical performance.

Keywords: metal organic frameworks; sandwich structure; spinel zinc cobalt oxide; graphene oxide; lithium ion batteries

1. Introduction

With the rapid development of electric vehicles and portable electronic devices, the increasing request for high energy storage devices promotes the development of lithium-ion batteries (LIBs) [1-2]. Graphite, as the mostly used

commercial anode material, exhibits a low theoretical capacity of 372 mAh g^{-1}, which can't meet the increasing demand for LIBs with higher reversible capacity and long cycle life[3]. In recent years, transitional metal oxides, especially cobalt-based oxides have drawn much attention for their potential application as anode materials duo to their much higher theoretical capacities[4-6]. However, their practical applications are hindered by their high cost and toxicity. Recently, tremendous efforts has been focused on spinel structured ternary cobalt-based oxides ($ZnCo_2O_4$[7-8], $NiCo_2O_4$[9-10], $MnCo_2O_4$[11-12], etc.), in which Co is partially replaced by less expensive and environmental friendly metals. Amongst these substitutions, zinc has been proved to exhibit good electrochemical performance as LIBs anode because it can store Li^+ through not only the conversion reaction but also the alloying reaction between Zn and Li ($Zn + Li^+ + e^- \rightleftharpoons LiZn$)[13-14]. However, the natural poor conductivity and the volume changes of spinel structured $ZnCo_2O_4$ anodes during Li^+ insertion/extraction processes hinder their industrial-scale application.

An efficient method to overcome the natural drawbacks is to fabricate composite with conductive buffer matrix. Among them, carbon materials are widely used and lead to remarkable improvement for the electrochemical performance. Zhang et al. fabricated $ZnMn_2O_4$/carbon aerogel composite, showing a great improvement of electrochemical performance in comparison with pure $ZnMn_2O_4$;[14] Fe_2O_3 nanoparticles uniformly distributed on reduced graphene oxide (RGO) exhibit improved electrochemical performance duo to the synergistic effect between MOs and RGO[15]. Fe_3O_4 nanospindles synthesized by Zhang et al. display enhanced cycling performance and rate capability by introducing carbon coating[16]. Carbon materials can not only greatly facilitate charge transfer, but also serve as cushion layer to buffer volume changes, thus resulting in notable enhancement of the electrochemical performance.

Recently, metal-organic frameworks (MOFs) or coordination polymers have drawn much attention for their applications as electrodes for LIBs. MOFs consisting of organic ligands and metal ions, can transform into carbon materials and metal species with proper methods. Carbon materials derived from MOFs by simply carbonization of organic ligand and removal of metal species have shown good electrochemical performance in lithium-sulfur batteries[17-18] and lithium-selenium batteries applications[19-20]. MOFs derived tailorable metal oxides or metal oxide/carbon nanomaterials with unique nanostructures exhibit outstanding electrochemical performance when used as LIBs anodes. Recently, spindle-like and cube-like porous Fe_2O_3 derived from MIL-88-Fe and Prussion Blue Nanocubes exhibit excellent electrochemical performance duo to their robust porous structure.[21-22] By using Zn-Co-ZIFs as precursors, Wu et al. fabricated porous spinel $Zn_xCo_{3-x}O_4$ polyhedra, exhibiting cycling stability and rate capability[23]. More recently, hetero-metal MOFs (Fe^{III}–MOF-5 and $Zn_3[Fe(CN)_6]_2$) were introduced to obtain hybrid architectures and the synergistic effect between $ZnFe_2O_4$ and ZnO results in excellent electrochemical performance[24, 25]. Though many kinds of MOFs have been used to synthesize various electrode materials, only a few works focus on MOF composite materials and their applications as electrode materials precursors for energy storage devices.[26-27] By simply composited with carbon nanotube and graphene oxide, MOFs derived metal oxides exhibit greatly enhanced electrochemical performance duo to the synergistic effect between metal oxides and carbon nanotube or reduced graphene oxide. Building proper MOFs composites is predictable an efficient way to enhance electrochemical performance of MOFs-derived productions.

Nickel foam is an attractive and commonly used current collector in lithium secondary batteries and capacitors. Active materials grown on nickel foam can be directly used as binder- and conductive-agent-free electrodes, thus

avoiding the complex procedures of electrode manufacture. However, probably owing to lack of effective synthetic methods, MOFs/Nickel foam composite is scarcely reported. In this paper, we first fabricated a novel hetero-metal MOF composite with nickel foam, GO/Zn-Co-ZIF/Ni, which was then transformed into RGO/$ZnCo_2O_4$-ZnO-C/Ni foam sandwich-like structure. The Zn-Co-ZIF derived products display typically porous polyhedron structure, which consists of interconnected carbon-coated $ZnCo_2O_4$-ZnO nanocrystals. While RGO nanosheets and Ni foam sandwich these porous polyhedrons between them, acting as two highways for charge transfer during discharge-charge processes. The interconnected carbon layers together fabricate a three dimensional conductive networks to wire up all the $ZnCo_2O_4$-ZnO nanoparticles, simultaneously acting as buffer layer for volume changes. The unique microstructure of polyhedrons and the novel design of sandwich-like structure promise excellent electrochemical performance when used as LIBs anodes.

2. Experimental Section

Fabrication of Zn-Co-MOF/Ni

Nickel foam was first washed with acetone, hydrochloric acid and deionized water to remove the possible oxide layer and organic species, and then dried in an electric oven. In a typical synthesis, 2.4 g polyvinylpyrrolidone (PVP, K30) was dissolved in 120 ml methanol, then the pretreated nickel foam was immersed into PVP solution under ultrasonication treatment for 30 minutes. Then 2.328 g $Co(NO_3)_2$•$6H_2O$ and 1.188 g $Zn(NO_3)_2.6H_2O$ were dissolved into the PVP solution to form a homogeneous solution named A. Subsequently, 2-methylimidazole (Aladdin, 98.0%, 3.936 g) was dissolved in 40ml methanol to form a clear solution B, followed by slowly addition into solution A under gentle agitation, then a dark blue solution C was obtained, with nickel foam hung in it. After mild stirring for 12h at room temperature, the nickel foam was taken out and washed with methanol. Then this nickel foam was once again immersed into another fresh solution C with mild stirring for 12h. After thoroughly washed with methanol for several times, the blue Zn-Co-ZIF/nickel foam was obtained. The obtained Zn-Co-ZIF is named as Zn-Co-ZIF-0.68[23], where the 0.68 indicates the Zn/Co molar ratio in the MOFs which is calculated from the XPS results below.

Fabrication of GO/ZIF/Ni and RGO/$ZnCo_2O_4$-ZnO-C/Ni sandwich structures

The coating of graphene oxide on MOF was derived by electrostatic force. Briefly, the surfaces of MOF crystals were firstly decorated by poly(diallyldimethylammoniumchloride) (PDDA) to gain positive charge surface. And then the negative charged graphene oxide nanosheets can easily be adsorbed onto the surface of MOF crystals. In a typical processes, 2.149 g PDDA solution (35%), 0.363 g tris and 0.173 g NaCl were dissolved in 150 ml deionized water to form a clear solution D. Then MOF/Ni was immersed in the stirring solution D for 30 minutes, followed by washing with deionized water for three times to remove the redundant PDDA. The decorated MOF/Ni was then immersed in GO solution under stirring for 30 minutes. After washed with deionized water for several times to remove the redundant GO, the GO/ZIF/Ni was obtained. Co-only ZIF-67 and Zn-only ZIF-8 were also synthesized through the same procedures except the use of metal precursors.

The fabrication of RGO/$ZnCo_2O_4$-ZnO-C/Ni was achieved by simply annealing of the as synthesized GO/ZIF/Ni at 450 ^oC for 3h with a heating ramp of 3 ^oC/min under N_2 flow in a tube furnace.

2.2 Material characterization

X-ray diffraction (XRD) patterns were collected using Rigaku D/Max-Rb diffractometer equipped with Cu Ka radiation (λ = 1.5406 Å). The morphology and components of the synthesized products were analyzed using

SU-70 field emission scanning electron microscopy (FE-SEM) and attached X-ray energy dispersive spectrometry (EDS), respectively. The morphology and structure of the synthesized products were analyzed using high-resolution transmission electron microscopy (HR-TEM) of JEM-2100 at an acceleration voltage of 200 kV. X-ray photoelectron spectroscopy (XPS) characterization was carried out in an ESCALAB 250 instrument with 150W Al Ka probe beam.

2.3 Electrochemical measurements

The electrochemical measurements were carried out by using 2025 coin-type cells, in which the RGO/$ZnCo_2O_4$-ZnO-C/Ni as working electrode, a lithium metal foil with size of 15.8mm*0.2mm as reference electrode, a celgard 2325 as separator and a solution of 1.0 M $LiPF_6$ in mixed EC and DEC (1:1 by volume) as the electrolyte. The mass of active materials in the electrodes is measured to be 1 mg. Fresh coin cells were assembled in an Ar-filled glove box. The cell were discharged and charged on LAND CT2001A battery test system from 3.0 V to 0.01 V under 25 ºC. Cyclic Voltammetry (CV) and electrochemical impedance spectroscopy measurements were carried out on an electrochemical workstation (PARSTAT 2273) at room temperature.

3. Results and discussions

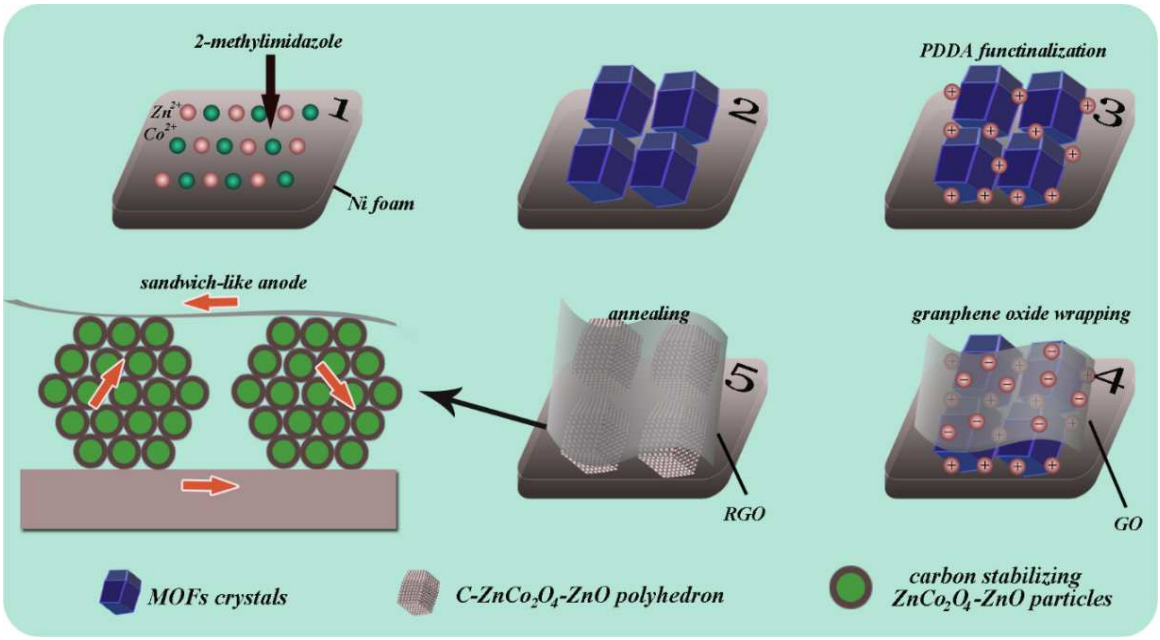

Figure 1. Schematic illustration for the formation of sandwich-like RGO/$ZnCo_2O_4$-ZnO-C/Ni electrode.

The synthesis strategy of Zn-Co-ZIF-0.68/Ni is schematically depicted in Figure 1. After thoroughly ultrasonic treatment in PVP solution, the surface of nickel foam is functionalized with PVP molecules. Then when the metal cations precursors are added, some Zn^{2+} and Co^{2+} cations are entangled on the surface duo to the interactions between PVP and cations[28-29] (Step 1). Subsequently, nucleation and growth of ZIFs occurs on the surface of nickel foam with the addition of 2-methylimidazole, resulting in the formation of ZIFs nanocrystals on the Ni surface (Step 2). Then the surface of ZIFs crystals is firstly functionalized with positive charges by PDDA, a

cationic polyelectrolyte[30] (Step 3). When ZIF/Ni is soaked in GO solution, negatively charged graphene oxide nanosheets are tightly absorbed onto the ZIFs surface duo to the electrostatic interactions between them, resulting in the formation of GO/ZIF/Ni sandwich-like structure (Step 4). Then after annealing at 450 ºC under N_2, graphene oxide transform into reduced graphene oxide, while ZIFs transform into N-doped carbon-coated metal oxides, leading to the formation of RGO/$ZnCo_2O_4$-ZnO-C/Ni sandwich-like structure.

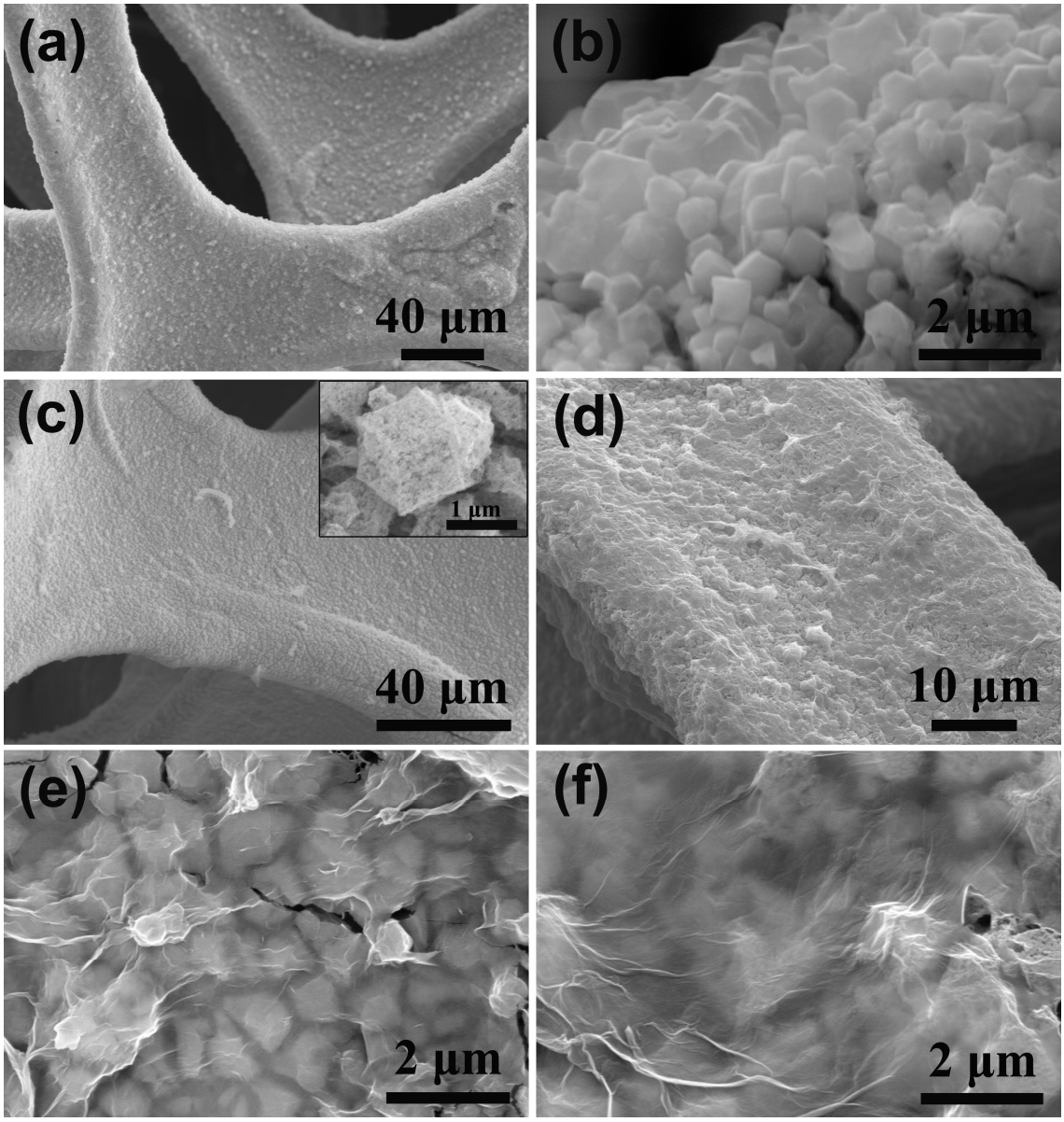

Figure 2. SEM images of (a) (b) Zn-Co-ZIF-0.68/Ni, (c) $ZnCo_2O_4$-ZnO-C/Ni, (d-e) GO/Zn-Co-ZIF-0.68/Ni, (f) RGO/$ZnCo_2O_4$-ZnO-C/Ni.

As shown in Figure 2a, MOF crystals are successfully grown on the surface of nickel foam with uniformly covering. Magnified SEM image (Figure 2b) shows that the size of the MOF nanocrystals is 0.6~1 μm. After functionalization with PDDA, the surface of the ZIF crystals is positively charged. Then the negatively charged

graphene oxide wraps on the surface of MOF crystals duo to the electrostatic interactions, forming a GO/ZIF/Ni sandwich-like structure. In Figure 2d, graphene oxide nanosheets with crinkled textures cover uniformly on the surface of ZIF crystals. Close observation (Figure 2e) confirms that chiffon-like graphene oxide nanosheets tightly wrap on the surface of ZIFs, and the MOF crystals are still visible through the wrinkled GO nanosheets.

After the annealing treatment of GO/ZIF/Ni at 450 ^{o}C under N_2 flow, the graphene nanosheets covered on the surface transform into reduced graphene oxide (RGO), which would facilitate charge transfer during electrochemical reactions. MOF crystals transform into $ZnCo_2O_4$-ZnO-C carbon/metal oxide composites duo to the pyrolysis of organic species and oxidation of metal species. The annealing treatment of ZIF/Ni framework without GO coating is also conducted, and a typical FESEM image is shown in Figure 2c. Porous polyhedrons of $ZnCo_2O_4$-ZnO-C on the surface of Ni foam are obtained after heating treatment. A close observation (Figure 2c inset) clearly reveals their porous structure. After graphene oxide nanosheets wrap on the surface of ZIFs, the heating production turns out to be RGO-wrapped porous polyhedrons. As shown in Figure 2f, porous polyhedrons grown on the surface Ni foam, are covered with chiffon-like RGO nanosheets. The active material porous $ZnCo_2O_4$-ZnO-C polyhedrons lie between two high conductive substrates, Ni foam and RGO nanosheets, forming a sandwich-like structure. The high conductive Ni foam and RGO nanosheets would simultaneously ensure two unobstructed highway for charge transfer, thus promising a good electrochemical performance, especially at high rates.

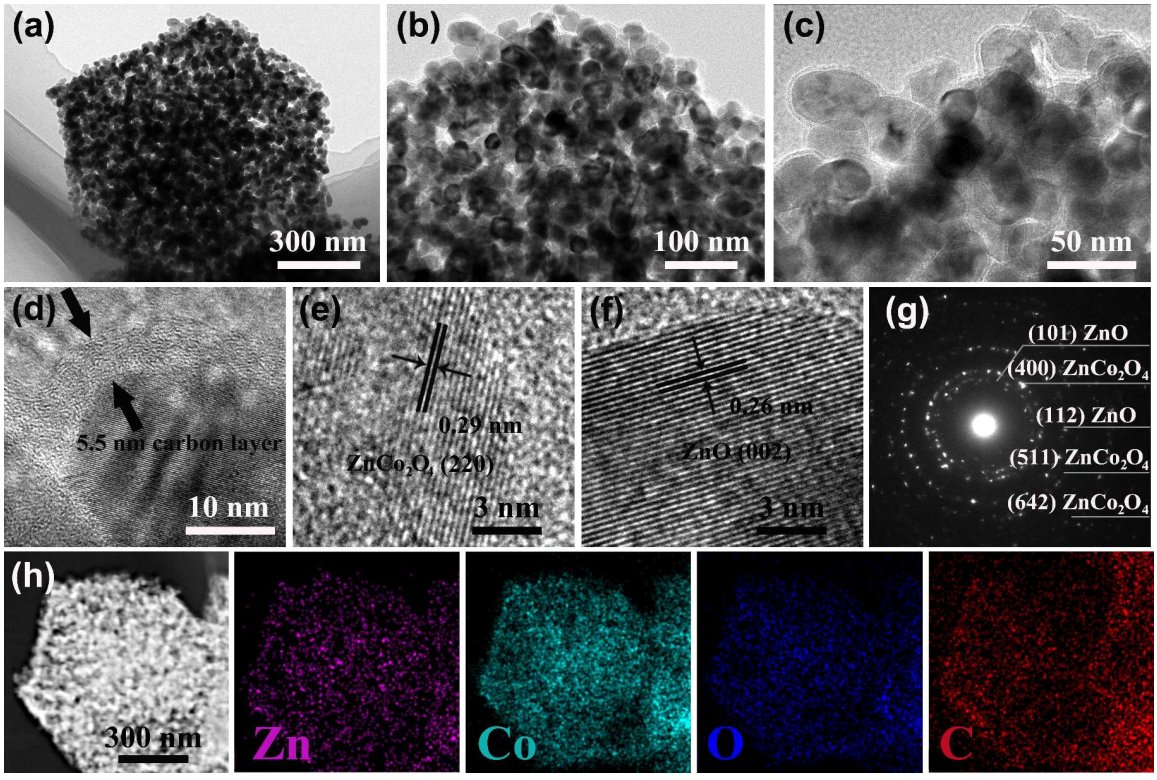

Figure 3. (a) (b) (c) TEM images, (d) (e) (f) HRTEM lattice images, (g) SEAD patterns, (h) Elemental mapping images of the C-$ZnCo_2O_4$-ZnO polyhedrons.

Transmission electron microscopy (TEM) is used to further investigate the microstructure of the polyhedrons. The low-magnification TEM images (Figure 3a-3b) confirm the porous structure of polyhedron, which consists of

interconnected nanoparticles. Further high-magnification TEM images (Figure 3c) reveal an average size of 50 nm for the nanoparticles, with void space between them. Interestingly, uniform carbon layer is observed to coat on the surface of metal oxide nanoparticles. This carbon layer is derived from the pyrolysis of the N-containing organic ligand 2-methylimidazole. The HRTEM image (Figure 3d) confirms a 5.5 nm thickness for the carbon layer. The lattice fringes of the metal oxides is clearly observed in HRTEM image (Figure 3e and 3f). The marked d-spacing of 0.29 nm corresponds to the (220) interplane spacing of $ZnCo_2O_4$ (PDF 23-1390), while 0.26 nm can be assigned to the (002) interplane spacing of ZnO (PDF 75-0576), demonstrating the metal oxide to be mixture of spinel $ZnCo_2O_4$ and ZnO. The diffraction rings in a selected area electron diffraction (SAED) pattern (Figure 3g) match well with (101), (112) planes of ZnO and (511), (400), (642) planes of spinel $ZnCo_2O_4$, further confirms the presence of $ZnCo_2O_4$ and ZnO. The elemental mapping analysis of porous $ZnCo_2O_4$-ZnO-C polyhedron (Figure 3h) confirms the homogeneous distribution of Zn, Co, O and C element among the porous polyhedron.

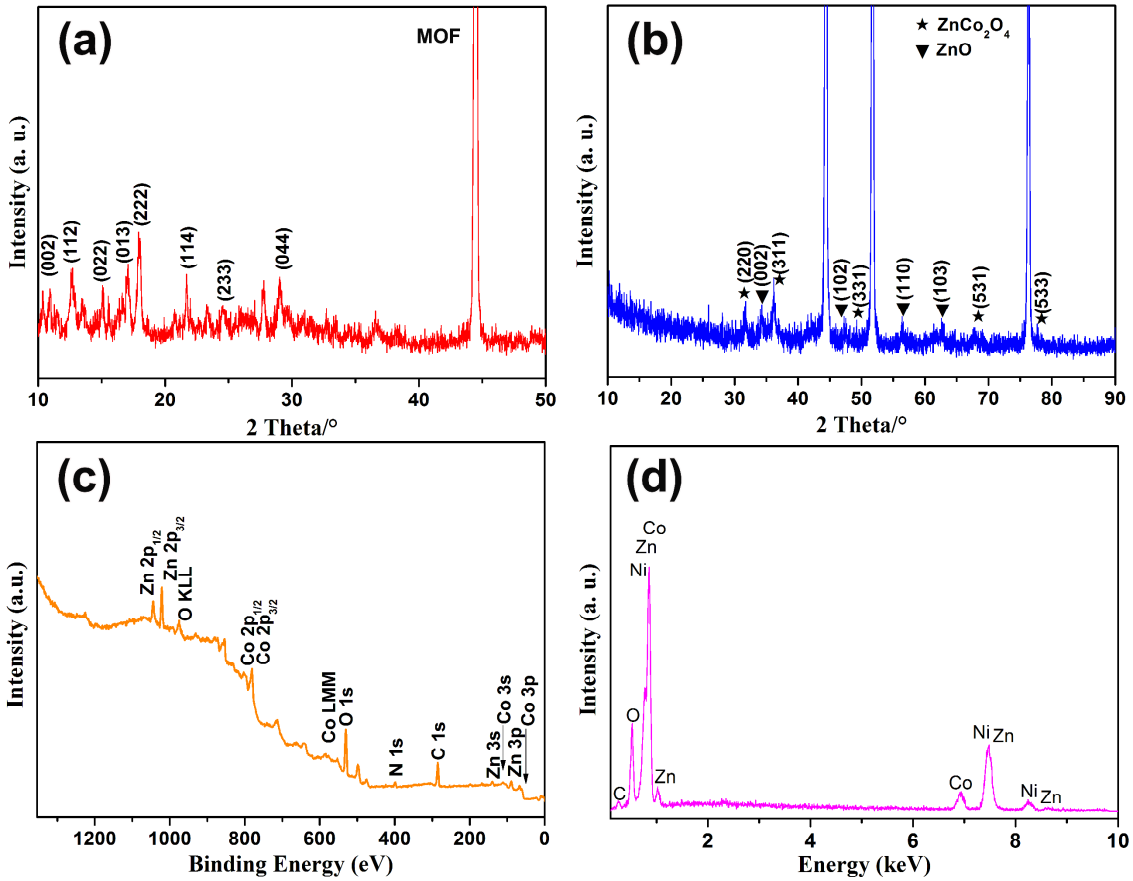

Figure 4. XRD patterns of the (a) GO/Zn-Co-MOF/Ni, (b) RGO/$ZnCo_2O_4$-ZnO-C/Ni samples. (c) XPS survey spectrum, (d) EDX spectrum of the RGO/$ZnCo_2O_4$-ZnO-C/Ni.

The phase component of the products is characterized by XRD patterns (Figure 4a: GO/ZIF/Ni; Figure 4b: RGO/$ZnCo_2O_4$-ZnO-C/Ni). The extremely strong diffraction peaks at 44.5°, 51.8° and 76.4° in Fig. 4b correspond to the (111), (200) and (220) peaks of Ni (PDF 70-1849), respectively. Besides XRD peaks, the other peaks of GO/MOF/Ni at positions lower than 50 degrees in Fig. 4a match well with the XRD pattern of previous reported ZIF-67[31], confirming the formation of ZIF-67 MOFs on the surface of nickel foam. For

RGO/$ZnCo_2O_4$-ZnO-C/Ni sample, although strong influence of the nickel substrate, some small peaks can still be recognized. The peaks located at 31.2°, 36.9°, 49.1°, 59.3° and 77.3 ° match well with (220), (311), (331), (531) and (533) of spinel $ZnCo_2O_4$ (PDF 23-1390), respectively, while the peaks at 34.4°, 47.6°, 56.6° and 63.0° correspond to (002) (102) (110) and (103) of hexagonal ZnO (PDF 75-0576), further confirming the coexistence of ZnO and $ZnCo_2O_4$.

The chemical component and chemical element valance of the synthesized production are investigated by X-ray photoelectron spectroscopy. As shown in Figure 4c, typical characteristic peaks of Zn, Co, O, C and N element are observed in the survey spectrum, confirming their existence in the composite. For the high resolution Zn 2p spectrum (Figure S1a), two peaks located at 1021.1 and 1044.2 eV correspond to Zn $2p_{3/2}$ and Zn $2p_{1/2}$, respectively, confirming the Zn (II) oxidation state[32]. In Co 2p spectrum (Figure S1b), two peaks located at 780.1 eV for Co $2p_{1/2}$ and 795.5 eV for Co $2p_{3/2}$ are observed, indicating the Co (III) oxidation state[32]. The peaks at 284.7 and 400.0 eV correspond to C 1s and N 1s, respectively. The C 1s peak confirms the existence of carbon layer coating on the surface of metal oxide, while the N 1s peak indicates the doping of N into the carbon layer duo to the nitrogen-containing organic ligand 2-methylimidazole. The molar ratio of Zn:Co is measured to be 1:1.48, which indicates the molar ratio of ZnO:$ZnCo_2O_4$ to be 1:2.84. The carbon proportion is measured to be 10.5 wt% by XPS. Energy dispersive X-ray analysis (EDX) (Figure 4d) also shows the coexistence of Zn, Co, O and C peaks, further demonstrating the elemental composition component of the porous polyhedron.

GO/ZIF-67/Ni and GO/ZIF-8/Ni composites are also synthesized and then transformed into RGO/CoO-C/Ni and RGO/ZnO-C/Ni composites. As shown in Figure S2 and S3, ZIF-67 with size of 1 μm and ZIF-8 crystals with size of 300 nm were successfully engineered on the surface of Ni foam. After GO wrapping and heating treatment, RGO/CoO-C/Ni and RGO/ZnO-C/Ni sandwich structure are obtained. XRD patterns (Figure S5a and 5b) confirm the metal oxides are CoO (PDF 71-1178) and ZnO (PDF 79-0208), respectively. EDS results (Figure S5c and d) of the CoO-C/Ni and ZnO-C/Ni reveal the existence of C in the composites, further confirming the composites are RGO/CoO-C/Ni and RGO/ZnO-C/Ni, respectively.

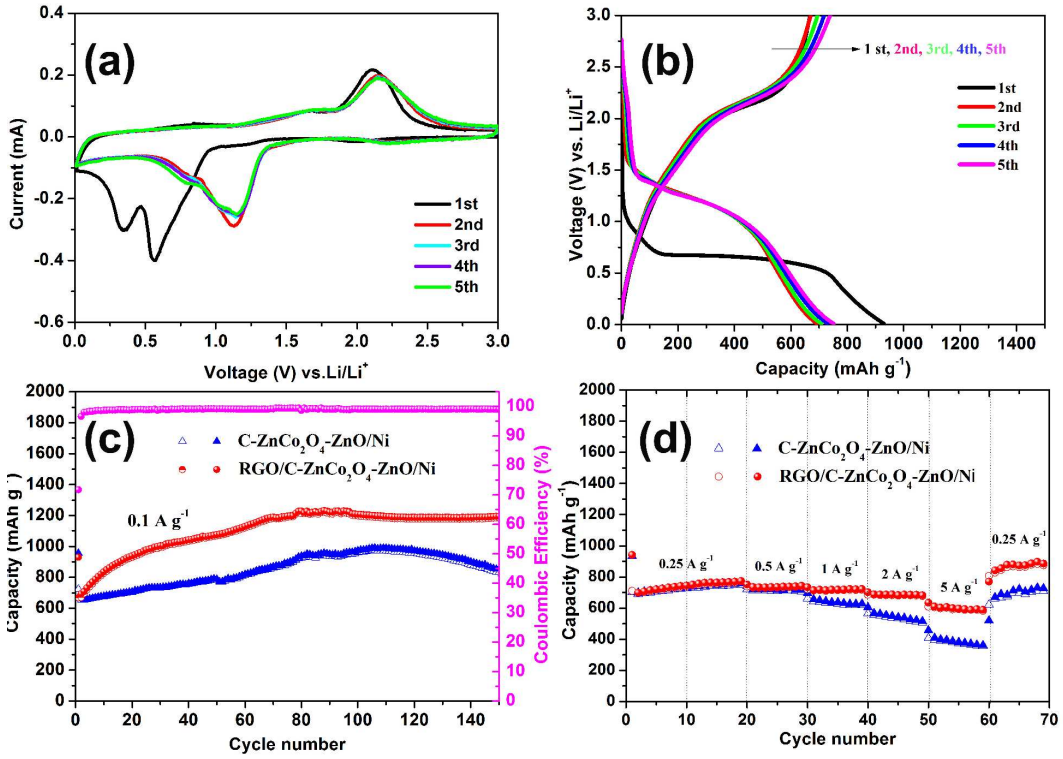

Figure 5. (a) CV curves of the RGO/$ZnCo_2O_4$-ZnO-C/Ni anode for five cycles at a scan rate of 0.1 mV s^{-1} in the voltage range of 3.0-0.01 V, (b) Discharge–charge profiles of the RGO/$ZnCo_2O_4$-ZnO-C/Ni at a current density of 0.1 A g^{-1} in the voltage range 3.0-0.01 V, (c) Cycling performance of RGO/$ZnCo_2O_4$-ZnO-C/Ni and $ZnCo_2O_4$-ZnO-C/Ni anode at 0.1 A g^{-1} (pink circles show the Coulombic efficiency of RGO/$ZnCo_2O_4$-ZnO-C/Ni, (d) Rate capabilities of RGO/$ZnCo_2O_4$-ZnO-C/Ni and $ZnCo_2O_4$-ZnO-C/Ni.

The RGO/$ZnCo_2O_4$-ZnO-C/Ni framework was punched into round discs and then assembled into 2025 coin cells without using any binders or conductive additives. Besides, Ni foam substrate is reported to make negligible contributions to the total capacity according to the previous reports[33-34]. Prompted by this unique sandwich structure, in which N-doped carbon coated $ZnCo_2O_4$-ZnO constructed porous polyhedrons are sandwiched between RGO nanosheets and Ni substrate, the electrode is expected to exhibit good electrochemical performance. Electrodes of RGO/CoO-C/Ni and RGO/ZnO-C/Ni were also assembled into coin cells for further investigation.

Figure 5a presents the first five CV cueves of the RGO/Polyhedron/Ni electrode at 0.1 mV S^{-1} between 0.01 V and 3 V. The CV curves of RGO/CoO-C/Ni electrode and RGO/ZnO-C/Ni electrode are shown in Figure S6. In the first cathodic scan of RGO/$ZnCo_2O_4$-ZnO-C/Ni, two strong peaks located at 0.6 V and 0.34 V are observed. While one peak between 0.25 and 0.4 V is observed for the RGO/ZnO-C/Ni (Figure S6b), corresponding to the initial processes of ZnO component. In a previous literature, the 0.34 V peak in the first cathodic scan is also explained to be the first electrochemical process of the ZnO material[35]. So the 0.34 V peak is ascribed to the initial electrochemical processes of ZnO component of $ZnCo_2O_4$-ZnO system, including the reduction of ZnO into Zn^0 and the formation of Li-Zn alloy.[35] And the 0.6 V peak can be due to the initial processes of $ZnCo_2O_4$ [36-37], including the decomposition of $ZnCo_2O_4$ to Zn^0 and Co^0 and the formation of SEI, so the 0.6 V peak is due to the initial electrochemical processes of $ZnCo_2O_4$ component of $ZnCo_2O_4$-ZnO system. In the anodic scan of ZnO electrode, several small oxidation peaks at 0-0.8 V correspond to a multistep dealloying process of Li-Zn alloy

(LiZn, Li_2Zn, $LiZn_2$, Li_2Zn_5), and the peak at 1.1-1.75 V should be related to the decomposition of Li_2O and formation of ZnO.[38-39] According to the previous literatures, $ZnCo_2O_4$ electrodes exhibit two broad oxidation peaks located at 1.7 V and 2.2 V, corresponding to the oxidation of Zn to Zn^{2+} and Co to Co^{3+}, respectively.[40-41] So the broad peak at 1.1-1.75 V for the $ZnCo_2O_4$-ZnO is ascribed to the oxidation of Zn to Zn^{2+} for both $ZnCo_2O_4$ and ZnO components. And the 2.2 V peak corresponds to the oxidation of Co to Co^{3+}. In the subsequent cycles, the main reduction peak of $ZnCo_2O_4$ shifts to 1.2 V. [42] This shift of peak position to higher potentials in the following cycles is also reported in other literatures,[7, 24, 26, 36, 40, 43] which may be due to the drastic lithium-driven structural or textural modifications[44]. The reduction peak between 0.4-0.75 V for RGO/ZnO-C/Ni electrode is related to the reduction of ZnO to Zn and the formation of Li_2O[38, 45]. So the small peak at 0.75 V for $ZnCo_2O_4$-ZnO corresponds to the reduction peak of ZnO. The small peak close to 0 V is often believed to be due to Li^+ intercalation into carbon materials (RGO and carbon layers)[46]. The CV profiles overlap well with each other in the 2nd~5th cycles, indicating a good electrochemical reversibility of the RGO/ $ZnCo_2O_4$-ZnO-C /Ni electrode.

Based on the above analysis, the main electrochemical reactions are believed to proceed as follows:

$$(1) ZnCo_2O_4 + 8Li^+ + 8e^- \rightleftharpoons Zn + 2Co + 4Li_2O$$

$$(2) ZnO + 2Li^+ + 2e^- \rightleftharpoons Zn + Li_2O$$

$$(3) Zn + Li^+ + e^- \rightleftharpoons ZnLi$$

$$(4) 6C + xLi^+ + xe^- \rightleftharpoons Li_xC_6$$

Galvanostatic discharge-charge experiment is conducted to evaluate the electrochemical performance of the RGO/$ZnCo_2O_4$-ZnO-C/Ni electrode at a current density of 0.1 A g^{-1} between 3 V and 0.01 V vs Li^+/Li. Figure 5b shows the discharge/charge profiles at 1st, 2nd, 3th, 4th and 5th cycle. For the initial discharge curve, a long plateau starting from 1.0 V and stabilizing at around 0.6 V can be observed, which is ascribed to the decomposition of $ZnCo_2O_4$ and ZnO into Zn^0, Co^0 and Li_2O, as well as the formation of solid electrolyte interphase (SEI) films. The initial discharge and charge capacity is 930.3 and 667.2 mAh g^{-1}, respectively, corresponding to an initial Coulombic efficiency of 71.7%. The irreversible capacity loss can be mainly attributed to the formation of solid electrolyte interphase. For the 2nd~5th cycles, the discharge profiles present a similar shape, showing a steeper discharge plateau between 1.45 V and 0.8 V, which is consistent with the CV curves. From the second cycle onwards, the coulombic efficiency improves remarkably, reaching 96.6% for the 2nd cycle (693.0 and 669.7 mAh g^{-1}) and achieving 98.3 % for the 5th cycle (751.7 and 739.1 mAh g^{-1}). Interestingly, the gradually increasing reversible capacities can be clearly revealed, with discharge capacities to be 693.0, 708.2, 731.3 and 751.7 mAh g^{-1} for the 2nd ~ 5th cycles, respectively. The gradually increasing reversible capacities during cycling can also be observed for some other transitional metal oxides anode materials, which may be ascribed to a gradual activation process of metal-oxide electrodes as well as reversible reactions between metal particles and electrolytes.

Figure 5c displays the cycle performance of the RGO/$ZnCo_2O_4$-ZnO-C/Ni sandwich-like electrode at 0.1 A g^{-1} for 150 cycles between 3 and 0.01 V. The $ZnCo_2O_4$-ZnO-C/Ni electrode without RGO wrapping is comparatively tested under the same condition to further confirm the important role of RGO. As is shown, for the RGO/Polyhedron/Ni electrode, a tendency of gradually increased reversible capacity is observed during the first

90 cycles, finally stabilizing at 1184.4 mAh g^{-1} for the 150th cycle, with a coulombic efficiency up to 99.1%. For comparison, polyhedron/Ni electrode without RGO wrapping also presents a gradually increasing capacities, reaching a capacity of 989.7 mAh g^{-1} at 110 cycle, with a relatively lower coulombic efficiency of 98.0%. A gradually capacity loss occurs in the subsequent cycles, finally reaching at a capacity of 854.9 mAh g^{-1} at the 150th cycle, exhibiting a relatively worse electrochemical performance. For the RGO/$ZnCo_2O_4$-ZnO-C/Ni sandwich-structured electrode, the RGO nanosheets act as not only a conductive substrate to wire up all the $ZnCo_2O_4$-ZnO-C polyhedrons, but also a flexible protector to fix them on the Ni foam, thus preventing their destroying and shedding during repeated discharge-charge processes.

Rate capabilities of RGO/$ZnCo_2O_4$-ZnO-C/Ni and $ZnCo_2O_4$-ZnO-C/Ni are also conducted under various current densities from 0.25 A g^{-1} to 5 A g^{-1} (Figure 5d). The RGO/$ZnCo_2O_4$-ZnO-C/Ni can exhibit 770.4 mAh g^{-1} at 0.25 A g^{-1} during the first 20 cycles. At higher current densities of 0.5, 1, 2 A g^{-1}, it can exhibit 738.1, 717.4, 677.8 mAh g^{-1}, respectively. Even at a high current density of 5 A g^{-1}, a high capacity of 588.2 mAh g^{-1} is still remained, showing excellent rate capabilities. Furthermore, the capacity can recover to 875.7 mAh g^{-1} when the current density reduced back to 250 mAh g^{-1}. However, for the Polyhedron/Ni without RGO wrapping, only 355 mAh g^{-1} is maintained at high rate of 5 A g^{-1}, exhibiting a worse rate capability.

The electrochemical impedance spectroscopy (EIS) measurements are also conducted to investigate the charge transfer kinetic properties at interface between electrode and the electrolyte. Each plot consists of a semicircle in the high-frequency region that attributed to the charge transfer process, and a sloping line in the low-frequency region corresponding to the diffusion of lithium ions[47]. As shown in Figure 6, the EIS spectrum of RGO/ $ZnCo_2O_4$-ZnO-C/Ni electrode shows a smaller diameter of the semicircles than that of $ZnCo_2O_4$-ZnO-C/Ni electrode, indicating a relatively lower charge transfer resistance. This result further confirms the role of RGO nanosheets during delithiation-lithiation processes. The covered RGO nanosheets wire up all the $ZnCo_2O_4$-ZnO-C polyhedrons, enhancing the charge transfer process during discharge-charge processes, resulting in good electrochemical performance, especially at high rates.

In a control experiment, we also investigate the electrochemical performance of RGO/CoO-C/Ni and RGO/ZnO-C/Ni. As shown in Figure S7, both of them exhibit worse electrochemical performance, only retaining 412.9 mAh g^{-1} and 177.2 mAh g^{-1} after 150 cycles for the RGO/CoO-C/Ni and RGO/ZnO-C/Ni, respectively. At a high rate of 5 A g^{-1}, only 90.6 mAh g^{-1} and 47.9 mAh g^{-1} can be remained, showing a worse rate capability of RGO/CoO-C/Ni and RGO/ZnO-C/Ni electrodes. So good electrochemical performance of the RGO/$ZnCo_2O_4$-ZnO-C/Ni electrode indicates the synergistic effects between the homogenously dispersed $ZnCo_2O_4$ and ZnO nanoparticles. The RGO/$ZnCo_2O_4$-ZnO-C/Ni composites can effectively relieve the crystal strain of each electrode domains caused by volume changes during electrochemical cycling, and the coexistence of highly dispersed ZnO and $ZnCo_2O_4$ nanoparticles can efficiently and spatially separate each other at the nanoscale, further preventing their self-aggregation, thus leading to enhanced electrochemical performance. [25, 48]

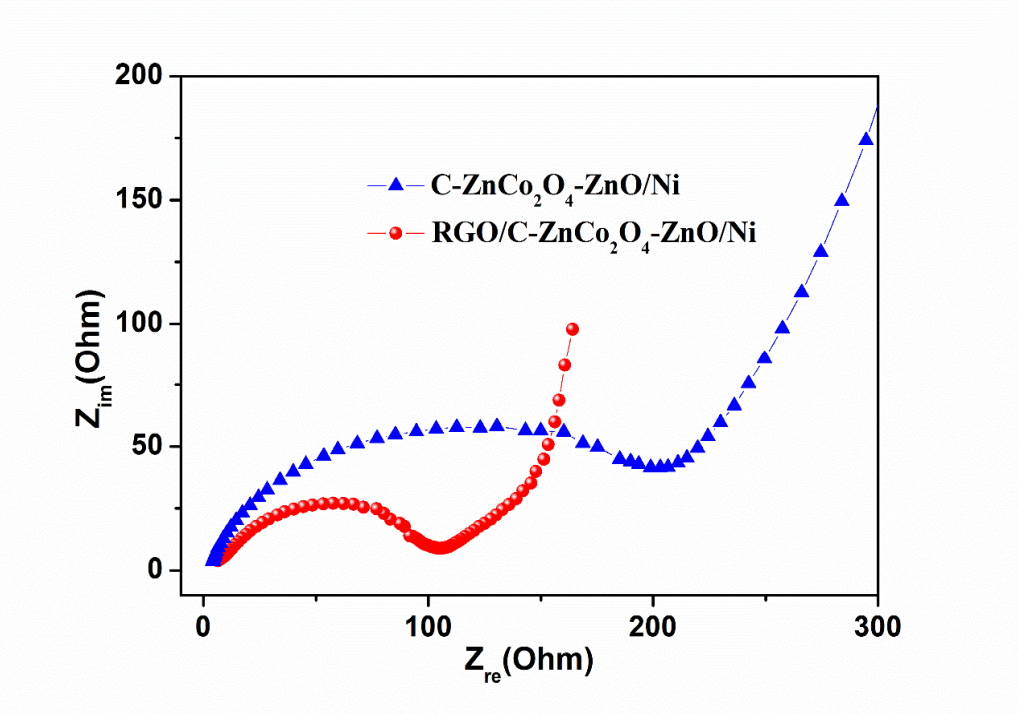

Figure 6. EIS spectrum of the $ZnCo_2O_4$-ZnO-C/Ni and RGO/$ZnCo_2O_4$-ZnO-C/Ni electrodes.

To further confirm the structural stability of the active materials during discharge-charge processes, the coin cells are disassembled after 150 cycles. Then after being washed and dried, SEM characterization was conducted, as is shown in Figure 6. It clearly shows that the sandwich-structure of RGO/$ZnCo_2O_4$-ZnO-C/Ni can be well retained after 150 cycles, without any collapse and shedding, indicating good structural stability of RGO/$ZnCo_2O_4$-ZnO-C/Ni. However, the $ZnCo_2O_4$-ZnO-C/Ni without RGO wrapping shows severe structural collapse and agglomeration after 150 discharge-charge processes (Figure S8c), and some active materials even shed from the Ni substrate, showing a bad structural stability of the $ZnCo_2O_4$-ZnO-C/Ni without RGO, which leads to the capacity loss after 110 cycles. RGO nanosheets play a crucial to prevent the active materials from collapsing, agglomeration and shedding, thus ensuring a good structural stability of the active materials.

The high specific capacity, good cycling stability and excellent rate capability of the RGO/$ZnCo_2O_4$-ZnO-C/Ni foam can be attributed to the unique microstructural features in the following several aspects. i) The MOF derived porous $ZnCo_2O_4$-ZnO-C nanocrystals ensure a short diffusion path of the lithium ions, thus ensuring a quick diffusion of the Li ions during extraction-insertion processes. ii) The in situ formation of carbon layer uniformly coated on the surface of the nanocrystals, can efficiently buffer the volume change of metal oxides during Li extraction/insertion processes. iii) Polyhedrons consisting of $ZnCo_2O_4$-ZnO-C nanoparticles possess abundant open pores in the polyhedron matrix, providing sufficient contact between electrolyte and active materials, as well as acting as cushion space to accommodate volume changes. iv) The high conductive RGO nanosheets wire up all the $ZnCo_2O_4$-ZnO-C polyhedrons. Furthermore, the thin carbon layers coated on porous $ZnCo_2O_4$-ZnO-C polyhedrons fabricate a three dimensional conductive matrix to wire up the $ZnCo_2O_4$-ZnO nanocrystals. The whole conductive network together provides an unhindered highway for charge transfer, thus exhibiting excellent electrochemical performance, especially at high rates. iiv) The wrapping RGO nanosheets also act as a flexible protector to fix $ZnCo_2O_4$-ZnO-C polyhedrons on the Ni foam, thus ensuring a good cycling stability.

Although a lot of works focus on MOFs derived metal oxides which exhibit good electrochemical performance as electrode materials for various energy storage devices, it's still valuable but challenging to achieve better electrochemical performance. Building proper MOFs composites is predictable to be an effective way. Recently, a MOF/Carbon nanotube composite (CNT) derived Co_3O_4/CNT composite exhibit 813 mAh g^{-1} at 100 cycles, which is much higher than the simple MOF derived Co_3O_4 (118 mAh g^{-1} at 100 cycles)[26]. A MOF/Graphene Oxide composite is fabricated by Qu and coworkers. This MOF composite derived Co_3O_4/RGO composite also exhibit greatly enhanced electrochemical performance (714 mAh g^{-1} at 200 cycles) than the pure Co_3O_4 electrode (511 mAh g^{-1} at 180 cycles).[27] It's evident that by building proper MOFs composites, electrochemical performance of MOFs derived materials can be greatly improved.

The GO/MOFs/Nickel foam composite we fabricated is new, and its derived RGO/$ZnCo_2O_4$-ZnO-C/Nickel foam sandwich-like structures also exhibit comparable or even better electrochemical performance than the previous reported general $ZnCo_2O_4$ nanomaterials[48-50] and even $ZnCo_2O_4$ materials on nickel foam[51], especially under high rates. The design of three dimensional carbon layer stabilized $ZnCo_2O_4$ nanoparticles sandwiched between double conductive RGO and nickel maximizes the electrochemical performance of active materials. And this new method to fabricate MOFs/nickel foam composite may also be inspiring for the synthesis of other similar materials used in various applications.

4. Conclusions

The porous $ZnCo_2O_4$-ZnO-C polyhedrons consisting of carbon coated $ZnCo_2O_4$-ZnO nanoparticles, are sandwiched between the highly conductive RGO and 3D porous Ni foam substrate. When acted as anodes for LIBs, the sandwich-structured anode exhibit good cycling stability, high specific capacity and excellent rate capability. The outstanding electrochemical performance is duo to the unique microstructures of andwich-like structure with RGO wrapped MOF-derived $ZnCo_2O_4$-ZnO-C polyhedrons on nickel foam. The $ZnCo_2O_4$-ZnO-C polyhedrons sandwiched between the highly conductive RGO and Ni substrate, can effectively ensure two highway for charge transfer during discharge/charge processes. The carbon layers on the surface of $ZnCo_2O_4$-ZnO nanoparticles act as buffer layers for volume changes. The open pores in polyhedrons not only guarantee large electrode-electrolyte contact area but also provide cushion space for volume changes. RGO nanosheets also serve as flexible protector to firmly fix polyhedrons on the Ni foam, ensuring a good cycling stability. We also envision that MOF based composites should be promising potentials for the high-performance LIBs anode and electrodes for other energy storage devices.

Acknowledgements

We acknowledge support from the National Natural Science Funds for Distinguished Young Scholars (No.: 51025211), National Nature Science Foundation of China (No.: 51472148, 51272137), the Tai Shan Scholar Foundation of Shandong Province.

References

[1] M. N. Obrovac, V. L. Chevrier, *Chemical reviews* **2014,** *114*, 11444-11502.

[2] Z. Wan, J. Shao, J. Yun, H. Zheng, T. Gao, M. Shen, Q. Qu, H. Zheng, *Small* **2014,** *10*, 4975-4981.

[3] H. Buqa, D. Goers, M. Holzapfel, M. E. Spahr, P. Novák, *J. Electrochem. Soc.* **2005,** *152*, A474-A481.

[4] P. L. Taberna, S. Mitra, P. Poizot, P. Simon, J. M. Tarascon, *Nat. Mater.* **2006,** *5*, 567-573.

[5] P. Poizot, S. Laruelle, S. Grugeon, L. Dupont, J.-M. Tarascon, *Nature* **2000,** *407, 496-499*.

[6] N. Du, H. Zhang, B. Chen, J. Wu, X. Ma, Z. Liu, Y. Zhang, D. Yang, X. Huang, J. Tu, *Adv. Mater.* **2007**, *19, 4505-4509*.

[7] G. Gao, H. B. Wu, B. Dong, S. Ding, X. W. D. Lou, *Advanced Science* **2015**, DOI: 10.1002/advs.201400014.

[8] L. Guo, Q. Ru, X. Song, S. Hu, Y. Mo, *J. Mater. Chem. A* **2015,** *3*, 8683-8692.

[9] L. Shen, L. Yu, X. Y. Yu, X. Zhang, X. W. Lou, *Angew. Chem., Int. Ed.* **2015,** *54*, 1868-1872.

[10] L. Shen, Q. Che, H. Li, X. Zhang, *Adv. Funct. Mater.* **2014,** *24*, 2630-2637.

[11] C. Fu, G. Li, D. Luo, X. Huang, J. Zheng, L. Li, *ACS Appl. Mater. Interfaces* **2014,** *6*, 2439-2449.

[12] A. K. Mondal, D. Su, S. Chen, A. Ung, H. S. Kim, G. Wang, *Chemistry* **2015,** *21*, 1526-1532.

[13] M. Yu, A. Wang, Y. Wang, C. Li, G. Shi, *Nanoscale* **2014,** *6*, 11419-11424.

[14] L. Yin, Z. Zhang, Z. Li, F. Hao, Q. Li, C. Wang, R. Fan, Y. Qi, *Adv. Funct. Mater.* **2014,** *24*, 4176-4185.

[15] X. Zhu, Y. Zhu, S. Murali, M. D. Stoller, R. S. Ruoff, *ACS Nano* **2011,** *5,3333-3338*.

[16] W.-M. Zhang, X.-L. Wu, J.-S. Hu, Y.-G. Guo, L.-J. Wan, *Adv. Funct. Mater.* **2008,** *18*, 3941-3946.

[17] Z. Li, L. Yin, *ACS Appl. Mater. Interfaces* **2015,** *7*, 4029-4038.

[18] K. Xi, S. Cao, X. Peng, C. Ducati, R. V. Kumar, A. K. Cheetham, *Chem. Commun.* **2013,** *49*, 2192-2194.

[19] Z. Li, L. Yin, *Nanoscale* **2015,** *7*, 9597-9606.

[20] Y. Lai, Y. Gan, Z. Zhang, W. Chen, J. Li, *Electrochim. Acta* **2014,** *146*, 134-141.

[21] X. Xu, R. Cao, S. Jeong, J. Cho, *Nano letters* **2012,** *12*, 4988-4991.

[22] L. Zhang, H. B. Wu, S. Madhavi, H. H. Hng, X. W. Lou, *J. Am. Chem. Soc.* **2012,** *134*, 17388-17391.

[23] R. Wu, X. Qian, K. Zhou, J. Wei, J. Lou, P. M. Ajayan, *ACS Nano* **2014,** *8,6297-6303*.

[24] F. Zou, X. Hu, Z. Li, L. Qie, C. Hu, R. Zeng, Y. Jiang, Y. Huang, *Adv Mater* **2014,** *26*, 6622-6628.

[25] L. Hou, L. Lian, L. Zhang, G. Pang, C. Yuan, X. Zhang, *Adv. Funct. Mater.* **2015**, *25*, 238-246.

[26] G. Huang, F. Zhang, X. Du, Y. Qin, D. Yin, L. Wang, *ACS Nano* **2015,** *9,1592-1599*.

[27] Q. Qu, T. Gao, H. Zheng, X. Li, H. Liu, M. Shen, J. Shao, H. Zheng, *Carbon* **2015,** *92*, 119-125.

[28] S. Lim, J. Cho, *Electrochemistry Communications* **2008,** *10*, 1478-1481.

[29] M. Liu, X. Yan, H. Liu, W. Yu, *Reactive & Functional Polymers* **2000,** *44, 55-64*.

[30] C. X. Guo, C. M. Li, *Energy Environ. Sci.* **2011,** *4*, 4504-4507.

[31] A. F. Gross, E. Sherman, J. J. Vajo, *Dalton transactions* **2012,** *41*, 5458-5460.

[32] T. F. Hung, S. G. Mohamed, C. C. Shen, Y. Q. Tsai, W. S. Chang, R. S. Liu, *Nanoscale* **2013,** *5*, 12115-12119.

[33] X. Li, A. Dhanabalan, K. Bechtold, C. Wang, *Electrochemistry Communications* **2010,** *12*, 1222-1225.

[34] J. M. Haag, G. Pattanaik, M. F. Durstock, *Adv. Mater.* **2013,** *25,*3238-3243.

[35] X. H. Huang, X. H. Xia, Y. F. Yuan, F. Zhou, *Electrochim. Acta* **2011,** *56*, 4960-4965.

[36] B. Qu, L. Hu, Q. Li, Y. Wang, L. Chen, T. Wang, *ACS Appl. Mater. Interfaces* **2014,** *6*, 731-736.

[37] Q. Xie, F. Li, H. Guo, L. Wang, Y. Chen, G. Yue, D. L. Peng, *ACS Appl. Mater. Interfaces* **2013,** *5*, 5508-5517.

[38] M. Ahmad, S. Yingying, A. Nisar, H. Sun, W. Shen, M. Wei, J. Zhu, *J. Mater. Chem.* **2011**, *21*, 7723-7729.

[39] M.-S. Wu, H.-W. Chang, *J. Phys. Chem. C* **2013**, *117*, 2590-2599.

[40] J. Bai, X. Li, G. Liu, Y. Qian, S. Xiong, *Adv. Funct. Mater.* **2014,** *24*, 3012-3020.

[41] W. Luo, X. Hu, Y. Sun, Y. Huang, *J. Mater. Chem.* **2012,** *22*, 8916-8921.

[42] S. H. Choi, Y. C. Kang, *ChemSusChem* **2013,** *6*, 2111-2116.

[43] G. Gao, H. B. Wu, S. Ding, X. W. Lou, *Small* **2015**, *11*, 432-436.

[44] Z. bai, Z. Ju, C. Guo, Y. Qian, B. Tang, S. Xiong, *Nanoscale* **2014**, *6*, 3268-3273.

[45] H. Wang, Q. Pan, Y. Cheng, J. Zhao, G. Yin, *Electrochim. Acta* **2009**, *54*, 2851-2855.

[46] X. Li, D. Geng, Y. Zhang, X. Meng, R. Li, X. Sun, *Electrochemistry Communications* **2011**, *13*, 822-825.

[47] Z. Li, B. Li, L. Yin, Y. Qi, *ACS Appl. Mater. Interfaces* **2014,** *6*, 8098-8107.

[48] M. A. Woo, T. W. Kim, I. Y. Kim, S.-J. Hwang, *Solid State Ionics* **2011***, 182*, 91-97.

[49] Y. Zhu, C. Cao, J. Zhang, X. Xu, *J. Mater. Chem. A* **2015,** *3*, 9556-9564.

[50] L. Guo, Q. Ru, X. Song, S. Hu, Y. Mo, *RSC Adv.* **2015,** *5*, 19241-19247.

[51] Y. Jin, L. Wang, Y. Shang, J. Gao, J. Li, X. He, *Ionics* **2015,** DOI 10.1007/s11581-015-1480-5.

[52] H. Long, T. Shi, S. Jiang, S. Xi, R. Chen, S. Liu, G. Liao, Z. Tang, *J. Mater. Chem. A* **2014,** *2*, 3741-3748.